AIAA JOURNAL
Vol. 48, No. 8, August 2010

Energy Deposition Applied to a Transverse Jet in a Supersonic Crossflow

Eli Lazar,* Gregory Elliott,† and Nick Glumac‡
University of Illinois at Urbana–Champaign, Urbana, Illinois 61801

DOI: 10.2514/1.J050050

An experimental investigation of a sonic underexpanded jet injected normally into a Mach 2.25 crossflow is reported. The jet exit geometry was circular and was operated at a jet-to-crossflow momentum flux ratio of 1.7. The unperturbed flowfield was analyzed with schlieren imaging, particle image velocimetry velocity data, surface oil flow visualizations, and pressure-sensitive paint measurements. As a means of excitation to the flowfield, an energy pulse from a *Q*-switched neodymium-doped–yttrium-aluminum-garnet laser was focused in the center of the jet exit at three different vertical locations. The focused laser pulse resulted in the induced optical breakdown of air, creating a plasma to perturb the flowfield. The perturbed resulting flowfield was analyzed with schlieren photography and particle image velocimetry. Analysis of phase-averaged schlieren images suggested that the resulting blast wave from the laser pulse disrupted the structure of the barrel shock and Mach disk. The two-component velocity field data revealed that the excitation pulse also caused a perturbation to the jet-shear layer and induced the formation of vortices that convect downstream.

Nomenclature

D	=	jet exit diameter
$\underline{D}^{2-D}$	=	two-dimensional equivalent form of local velocity gradient tensor
J	=	jet-to-freestream momentum flux ratio
M_j	=	Mach number at jet exit
M_∞	=	crossflow freestream Mach
P_j	=	pressure at jet exit
P_∞	=	crossflow static pressure
U_{avg}	=	average streamwise velocity
U_c	=	streamwise convective velocity
U_{RMS}	=	rms of streamwise velocity
U_∞	=	crossflow freestream velocity
u_1	=	streamwise velocity component
u_2	=	transverse velocity component
V_{avg}	=	average transverse velocity
V_{RMS}	=	rms of transverse velocity
X	=	streamwise positional coordinate
x_1	=	streamwise positional coordinate
x_2	=	transverse positional coordinate
Y	=	transverse positional coordinate
γ_j	=	specific heat ratio at jet exit
γ_∞	=	crossflow specific heat ratio
δ_{99}	=	boundary-layer thickness at 99% of freestream velocity
λ_r	=	real eigenvalue
λ_{cr}	=	real component of a complex eigenvalue
λ_{ci}	=	complex component of complex eigenvalue (also called swirling strength)
$(\lambda_{ci})^{-1}$	=	period required for a particle to swirl once about the λ_r axis

Presented as Paper 2009-1534 at the 47th AIAA Aerospace Sciences Meeting and Exhibit, Orlando, FL, 5–8 January 2009; received 7 July 2009; revision received 8 March 2010; accepted for publication 11 April 2010.

*Graduate Student, Department of Mechanical Science and Engineering, 104 S. Wright Street. Student Member AIAA.

†Professor, Department of Aerospace Engineering, 104 S. Wright Street. Associate Fellow AIAA.

‡Professor, Department of Mechanical Science and Engineering, 1206 W. Green Street. Member AIAA.

I. Introduction

THE transverse (normal) injection of a gaseous jet into a supersonic freestream is a fluid dynamic configuration that has been studied extensively due to its widespread use in a variety of technological applications [1]. Early investigations in the area were motivated by the aerodynamic control of supersonic vehicles at high altitude, forming initial qualitative descriptions for the structure of the resulting flowfield [2,3]. Of particular relevance to the current study is the use of this flowfield in high-speed propulsion systems. Because of the high velocities in these systems, challenges arise in the fuel injection method that must provide sufficient fuel–air mixing in an environment with limited flow residence time in the combustor [4]. As a means of addressing this problem, past studies have investigated the arrangement of the transverse injection of fuel from a wall orifice to evaluate near-field mixing and methods of enhancing it [5].

A jet injected normally from a wall into a crossflow involves two fundamental flows: a perpendicular free jet and a boundary layer driven by uniform flow far above the injection wall. However, the characteristics of the transverse jet are far more complex than those present in these basic canonical flows [6]. Figure 1 [5,7] illustrates the typical flowfield characteristics of an underexpanded transverse sonic jet injected into a supersonic crossflow. The displacement of the crossflow by the jet induces a three-dimensional bow shock, due to the partial blockage of the flow [8]. The bow shock causes the upstream wall boundary layer to separate, creating a region where the boundary layer and jet fluids mix at subsonic speeds, upstream of the jet exit. This region, confined by the separation shock wave formed in front of it, is important in transverse injection flowfields, owing to its flame-holding capability in combusting situations [5].

Turning to the internal structure of the jet, after leaving the wall orifice, the underexpanded jet initially expands through a Prandtl–Meyer expansion fan centered at the nozzle lip [8]. In the case of circular injector ports, this expansion terminates in a barrel-shaped shock and a Mach disk. The upstream separation region creates a horseshoe-shaped vortex that wraps around the injector exit along the wall [9]. The majority of the jet fluid passes through the oblique shocks that define the sides of the barrel shock and form an annular shear layer between the jet plume and the crossflow. Recirculation regions are located just upstream and downstream of the jet orifice, near the wall. The velocity field within the jet plume downstream of the barrel shock is dominated by two streamwise-oriented counter-rotating vortices [8].

Mixing properties of normal injection into supersonic flow are controlled by jet vortical structures [5]. Following the work of Ben-Yakar et al. [5], experimental studies by Fric and Roshko [10] of

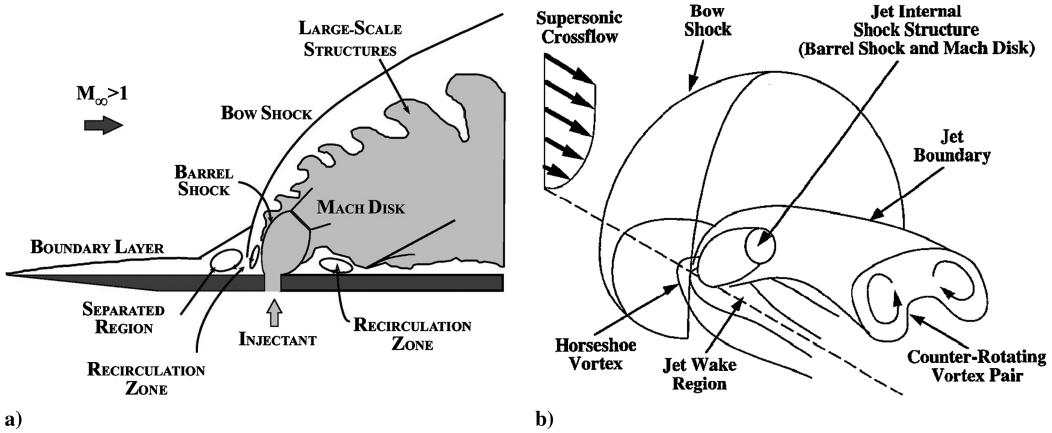

Fig. 1 Illustration of an underexpanded transverse injection into a supersonic crossflow for a) instantaneous side view and b) a three-dimensional perspective of averaged features (images from [5,7]).

a transverse jet injected into a low-speed crossflow have given insight into the characterization of these flowfield features. In particular, four types of coherent structures were discerned: 1) near-field jet-shear layer vortices, 2) the horseshoe vortex that wraps around the jet column, 3) the far-field counter-rotating vortex pair, and 4) the downstream wake vortices originating from the horseshoe vortex. An illustration of the presumed structure for a transverse jet in a supersonic crossflow is shown in Fig. 1. Figure 1 was taken after Ben-Yakar et al. [5], where the vortical structures were partially observed by numerous studies [11–13].

The near-field mixing of transverse jets is predominantly controlled by an entrainment-stretching-mixing process, which is driven by large-scale jet-shear layer vortices. Near the jet exit, the injected fluid moves with a higher velocity tangent to the interface than the freestream fluid. This effect leads to the periodic formation of large-scale vortices that engulf large quantities of freestream fluid and draw it into the jet-shear layer. These vortices also act to stretch the interface between the unmixed fluids. More specifically, stretching increases the interfacial area and steepens the local concentration gradient along the entire surface while enhancing the diffusive micromixing. Work by Ben-Yakar and Hanson [14] has shown that the far-field eddies reach velocities near the freestream velocity as they fully align with the freestream flow. This result was also previously shown by Gruber et al. [13]. For high-speed freestream conditions, the large-scale coherent structures, where the fuel and air are mixed by slow molecular diffusion, will also convect at high speeds, suggesting that the combustion process will be mixing-controlled [5]. Accordingly, understanding of the mixing process and its enhancement presents a critical component in the development of air-breathing propulsion systems for use in hypersonic flight.

In addition to the mixing characteristics of the flowfield, simultaneous penetration of the fuel jet into the high-speed crossflow must also be achieved to ensure efficient combustion [15]. Penetration has been shown to be primarily dependent on the jet-to-freestream momentum flux ratio J, which is expressed by

$$J = \frac{(\gamma P M^2)_j}{(\gamma P M^2)_\infty} \tag{1}$$

where the subscript j corresponds to the jet exit conditions and ∞ to the freestream conditions upstream of the bow shock. In Eq. (1), γ is the specific heat ratio, P is the pressure, and M is the Mach number. Work conducted by Billig et al. [16] (as well as other researchers) has identified the jet-to-freestream momentum flux ratio as the most important parameter for determining jet penetration. However, exceptions under different conditions/configurations may exist [5].

In an effort to further understand the mechanisms of mixing in a jet in crossflow, as well as to gain further insight into the physics of the flowfield, there have been a vast number of experimental and computational investigations. In a recent numerical study by Kawai and Lele [17], an underexpanded sonic jet injection into a supersonic crossflow was considered, using high-order compact differencing/filtering schemes coupled with the recently developed localized artificial diffusivity methodology in the context of large-eddy simulation. For their study, flow conditions from the experiment by Santiago and Dutton [18] were selected ($M_\infty = 1.6$). To that end, the simulation by Kawai and Lele [17] qualitatively reproduced the unsteady dynamics of the barrel shock and bow shock, as observed in the experiment. With regard to the processes controlling the jet mixing, two regions of vortex formation that create hairpinlike structures were identified in the windward and leeward jet boundaries, and these vortices played an important role in determining the behavior of jet fluid stirring and subsequent mixing.

In a another numerical study conducted by Srinivasan and Bowersox [9], simulations were conducted for a sonic transverse jet in Mach 2 and Mach 5 crossflows, using diamond-shaped orifices. The authors report that two new vortex features were observed in the vicinity of the injector port when compared with circular injector ports. First, a pair of vortices was seen to form near the leading edge of the injector, due to the corner vortices in the injector port and the interaction between the freestream and injector fluids. Of particular interest is the potential for these structures to serve as a mixing enhancement mechanism. Second, their investigation found that the shape of the barrel shock generated by the diamond-shaped injector influenced the flow around the injector port, leading to the formation of a vortex pair downstream of the injector port. They report that this induced flow structure can act as a flame-holding device.

In other related experimental work, a study conducted by VanLerberghe et al. [8] investigated a sonic jet injected normally into a Mach 1.6 crossflow. Shadowgraph photography and planar laser-induced fluorescence from acetone were used to obtain a temporally resolved flowfield visualization of a side view of the barrel shock region, a side view of the downstream plume, and an end-view cross section of the plume. The mixing produced by large-scale turbulent structures was analyzed by instantaneous images, mean and standard deviation images, and image-intensity probability density functions. Comparisons of the instantaneous images and probability density functions illustrated the role of large-scale rolling structures and jetlike plumes in transporting coherent packets of fluid across the three-dimensional shear layer formed between the jet and crossflow. Significant instantaneous mixing in the flowfield occurred in the wake region downstream of the barrel shock region and below the jet centerline. They also reported that the counter-rotating streamwise vortex pair in the jet plume played an important role in the scalar mixing processes, as it transports jet fluid down toward the wake and entrains crossflow fluid from below, up into the jet.

In another experimental study by Ben-Yakar et al. [5], the temporal evolution, the penetration, and the convection characteristics of hydrogen and ethylene sonic jets in a Mach 3.38 crossflow were investigated. These conditions were selected to simulate a supersonic

combustor environment associated with a hypersonic air-breathing engine flying at Mach 10. The experiment was conducted with ultrafast schlieren framing and performed for a similar jet-to-freestream momentum flux ratio between the two gases (hydrogen and ethylene). Observations made in their study illustrated distinct differences in the jet structure when the jet densities were relatively different. While, previously, the momentum flux ratio was considered to be the main controlling parameter in the jet penetration, their work suggested a significant result by demonstrating the existence of an additional mechanism that altered the penetration; vortical structures and mixing properties of the jet-shear layer were also shown to be affected. An increased penetration depth of nearly 50% was seen when ethylene was used at the injectant instead of hydrogen, even with the same momentum flux ratio and same crossflow Mach number. Contrasts in the jet structure could be due to the large differences in the jet exit velocity (between ethylene and hydrogen) to accomplish the same J values. An alternative explanation could be due to the large differences in jet densities.

As part of the work by Ben-Yakar et al. [5], the authors suggested that there would be value in identifying other mechanisms or controlling parameters, other than the jet-to-freestream momentum flux, which may alter the large-eddy characteristics of the jet-shear layer and, therefore, affect near-field mixing in realistic conditions. In an attempt to also contribute to this effort, we report an experimental study on the influence of pulsed energy deposition through laser-induced optical breakdown on the characteristics of a transverse sonic jet in a supersonic crossflow.

II. Experimental Setup

In the current experimental study, a transverse sonic jet in a crossflow was investigated using a supersonic blowdown wind tunnel. The tunnel was operated with good flow quality (i.e., in absence of strong compression or expansion waves in the test section) at a Mach number of 2.25. Air was supplied from a compressor with a volumetric flow rate of 34 m^3/min and at a pressure of 1000 kPA. The flow from the compressor was filtered, dried, and cooled, and it was stored in a 140 m^3 tank farm. From this point, the air traveled through a pipe and a series of control valves before entering the wind tunnel. Before reaching the test section, the flow passed through a conventionally arranged settling chamber with a honeycomb filter to reduce the scale of the incoming turbulence and to straighten and make the flow uniform. After leaving the test section, the flow entered the diffuser, which was approximately 91.4 cm long and sloped at 2.5°. This diffuser exhausts through a bent pipe wrapped in sound insulation and then through a silencer to the atmosphere [19].

The test section used for investigation had a square geometry, measuring 63.5 mm on each side. There were also two large windows ($119.1 \times 239.7 \times 25.4$ mm) on each side of the test section and a smaller bottom window ($36.5 \times 163.5 \times 19.1$ mm). Each of the windows was fabricated with a BK-7 grade A glass to provide high optical quality. The top of the test section was constructed with a polycarbonate resin thermoplastic (LEXAN), in which a circular round jet was installed. The jet geometry included a contoured nozzle to make the flow sonic and then ended into a 3.2-mm-long straight pipe. The exit diameter of the jet D was 4.8 mm and was operated with air as the working fluid. From Eq. (1), this gave a jet-to-freestream momentum flux ratio of $J = 1.7$. A full description of the wind tunnel can be found in [19], and relevant flow condition parameters have also been summarized in Table 1.

As a means of applying excitation to the flowfield, pulsed energy deposition from a Q-switched neodymium-doped–yttrium-aluminum-garnet (Nd:YAG) laser was used. The laser was operated at a wavelength of 532 nm, delivering approximately 200 mJ per pulse at a frequency of 10 Hz. The energy generated from the laser pulse was manipulated using a series of lenses, expanding the incoming beam diameter from approximately 9 to 20 mm and then focusing it to a point. Using this setup, the diffraction-limited spot size was on the order of 3 μm but, with real optical effects, the size is more on the order of 10^2 μm.

Table 1 Summary of experimental test conditions

Parameter	Value
Freestream stagnation pressure	276 ± 3 kPa
Freestream boundary-layer thickness	3.05 ± 0.13 mm
Freestream Mach number	2.25
Jet stagnation pressure	378 ± 13 kPa
Jet-to-freestream momentum flux ratio	1.7
Jet exit Mach number	1
Jet exit diameter	4.8 ± 0.05 mm

This optical arrangement resulted in the induced optical breakdown of air, providing a single burst of excitation by ionizing the flow and creating plasma. The excitation was applied at three vertical positions (relative to the jet exit) within the flowfield. These included vertical distances of 0, 1.5, and 3 jet diameters from the jet exit and in each case along the jet centerline. The resulting flowfield was analyzed with schlieren photography and particle image velocimetry (PIV). For the unperturbed flowfield, additional diagnostics of pressure-sensitive paint (PSP) measurements and surface oil flow visualizations were also conducted.

The schlieren system was setup in a standard Z arrangement. Illumination was provided by a Xenon spark lamp, which acted as a point light source, providing high luminance and emitting a broadband light. The generated light was then collimated through the wind-tunnel test section and focused to a point. Instantaneous schlieren images were recorded in the vertical and horizontal knife-edge configuration with a scientific-grade 1600×1200 pixel charge-coupled device (CCD) camera; the CCD camera was also used for each of the diagnostics described next. The duration of each flash for the spark lamp was on the order 20 ns, which resulted in conditions short enough to freeze most of the turbulent structures and produce instantaneous images of flow [20].

Two-dimensional PIV measurements were conducted to obtain quantitative velocity fluctuation data. The crossflow and jet were individually seeded with diethylhexyl sebacate (DEHS) through the use of separate Laskin nozzles that generated particles with diameters of less than 1 μm [21]. For both flows, seeding was introduced approximately 3.5 m upstream of the test section, which resulted in a sufficient dispersion of the particles. The particles were illuminated by a thin (on the order of 0.1 mm) light sheet. The light sheet was created by a dual-head New Wave Nd:YAG laser in conjunction with spherical and cylindrical lenses. The light sheet was brought in through the bottom access window of the test section and exited through the top section constructed of LEXAN. This design allowed particles near the surface to be recorded without saturating the CCD camera. An illustration of the setup is shown in Figs. 2a and 2b. The PIV laser was operated at a frequency of 532 nm, with each pulse delivering approximately 50 mJ of energy. The time separation between the laser pulses to illuminate the DEHS particles was adjusted according to the flow velocity and camera magnification. For the results shown in the present work, a separation time of approximately 600 ns was used.

The PIV system with an intensified CCD camera was also used to generate two-dimensional images containing mixing information. For this technique, the jet was seeded with ethanol particles that underwent a phase change from gas to solid as they accelerated into the freestream due to the drop in temperature and pressure. The ethanol particles then scattered laser light into the camera. Using this method, 50 run images and 50 background images were recorded and analyzed to mark the penetration boundary profile of the jet. Past studies [7] using similar diagnostics indicated that small condensed particles can easily follow the turbulent fluctuations within the flowfield.

The accuracy of velocity measurements obtained from the PIV data was a composite of the ability of the seed to follow the flow and, for the imaging and analysis system, to record and process a field of particle images [22]. In quantifying the accuracy, a number of factors need to be considered, such as the number of samples, turbulence intensity, computational algorithm, equipment used, and particle size

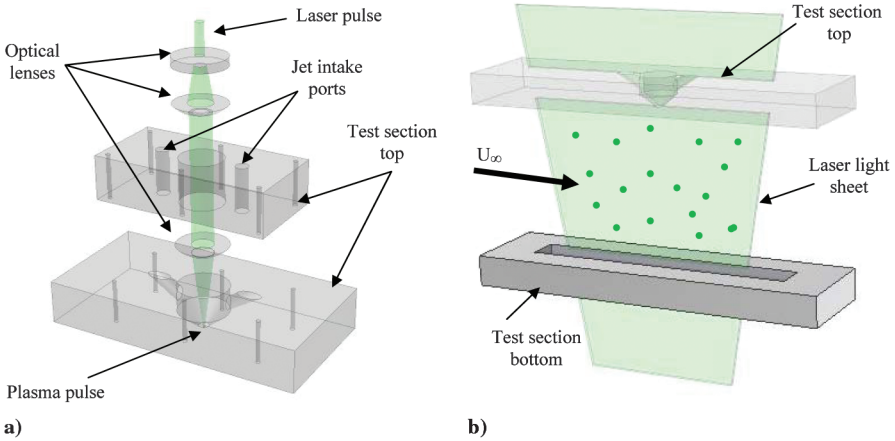

Fig. 2 Schematic of a) the jet and excitation arrangement and b) PIV setup.

[20]. In an effort to quantify some of these factors, several sources of error were considered. The error in timing between two laser pulses was estimated to be 6 ns. The uncertainty in pixel displacement by correlation analysis of the PIV software program was approximated at one-10th of a pixel, assuming the laser sheet is providing Gaussian illumination. Subpixel accuracy was achieved by matching the intensity captured from illuminated particles through a Gaussian-shaped peak locator, resulting in a positional error estimate of approximately 0.1 pixel [23].

For the mean flow, another source of error in the PIV data is due to the turbulence, which requires averaging of multiple images to obtain accurate mean properties. Using the approach outlined by Grant and Owens [24] and following the work of Zhuang et al. [20], the relative error in the mean velocity from sample averaging was estimated at up to 2.6% for the unperturbed flowfield velocity data and for a 95% confidence level. This value was based on the maximum turbulence intensity observed in the shear layer ($U_{\text{RMS}}/U_\infty = 0.35$, discussed next) and the averaging of 680 image pairs. This also translates to an uncertainty of no more than 8.3% for the turbulence intensity measurements. The uncertainty is slightly increased for the velocity data with forcing applied, as fewer images pairs were used for sampling averaging.

PSP measurements were conducted to investigate the static pressure distribution on the surface in the near-jet region. For this diagnostic, the surface surrounding the jet exit was coated in a paint consisting of organic luminophores suspended in polymeric binders. The luminophores were excited using a blue light-emitting diode (LED) lamp as an illumination source. The LED lamp was fitted with a low-pass filter so that the incident light in the range of the luminescent signal wavelength was mostly filtered. The intensity of the fluorescence from the PSP was captured with a CCD camera equipped with a 50 mm lens and a 610 nm high-pass filter to separate the fluorescent signal from the paint from that of the light source. The spatial resolution of the PSP surface measurements was calculated to be 59.9 μm/pixel, or approximately 278 pressure measurements per square millimeter. Fifty run images and 50 reference images were acquired for the results presented. Each sequence was ensemble-averaged, and the background noise was subtracted to provide a single run image. Following the experiment, pressure tap measurements were taken at five selected locations using transducers and correlated to the corresponding PSP intensity values to form a calibration curve. The locations of the tap sites were selected to include a wide range of pressures (approximately 1–8 psia), thereby minimizing errors introduced through extrapolation. The resulting calibration curve was constructed with a second-order polynomial and had a correlation coefficient of $R^2 = 0.999$. The maximum deviation of the pressures at the tap sites to the calibration curve was approximately 0.12 psia.

Finally, surface oil flow visualizations were performed by using a surface tracer mixture consisting of oleic acid, titanium dioxide, and silicon oil. The mixture was applied with a standard foam brush, covering the entire surface far upstream and downstream of the jet exit. Images of the surface were then recorded with a CCD and in ambient light.

III. Results

A. Surface Oil Flow Visualization

Surface flow visualization experiments were performed as a means of investigation of the streak lines surrounding the jet exit. Using this technique, instantaneous images of the surface for the unperturbed flowfield were recorded. A selected image is shown in Fig. 3, for which the tunnel was operated long enough for steady-state surface flow patterns to develop. In Fig. 3, the streamwise and transverse positional coordinates (X, Y) have been nondimensionalized by the jet diameter. The jet exit is located at the positional coordinates of (0, 0). As shown by Fig. 3, the surface flow pattern displays expected symmetry about the tunnel midline and also indicates that the near-jet region was not affected by the influence of the wind-tunnel side walls. There are several separation lines that can be identified in Fig. 3 and have been labeled 1–4. Following the work of Everett et al. [25], lines 1 and 2 can be seen to wrap around the injector port. The distinctive shape of these lines has led investigators to commonly refer to the vortex system resulting from the flow separation in this region as the horseshoe vortex. Consistent with the work by Everett et al. [25], the oil between lines 1 and 2 was observed to move outward and around the jet and not penetrate the boundary of either line. By comparison with the velocity data taken from the present work, lines 1 and 2 appear to correspond to the approximate position of the lambda shock and bow shock, and line 3 corresponds to the barrel shock.

Also shown in Fig. 3, immediately downstream of the jet exit, a point was observed where oil accumulated and then two separation lines emerged. These lines are labeled as 4 in Fig. 3. Again, similar to the work by Everett et al. [25], these lines appeared to represent a boundary between the reattaching flow downstream of the jet exit and the fluid upstream of the exit that moved around the jet. The lines initially diverge with increasing downstream position, until reaching

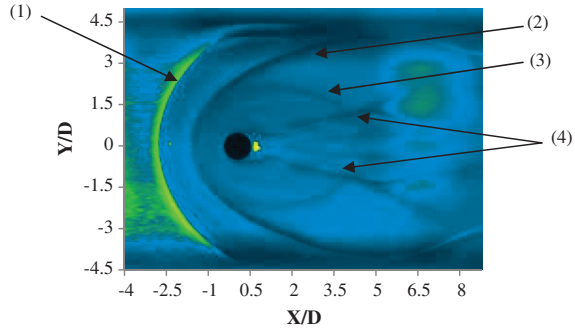

Fig. 3 Surface flow oil visualizations of a transverse sonic jet in a supersonic crossflow, where labels 1–4 mark separation lines.

a location of approximately $x/D = 5$, after which they were observed to converge slightly.

B. Pressure-Sensitive Paint

PSP was applied to the near-jet region to obtain qualitative information for the surface pressure distribution generated by the transverse jet flowfield. A color contour plot of the resulting distribution of the absolute surface pressure is shown in Fig. 4. In Fig. 4, the flow direction is from left to right, where the jet exit is represented by the dark circular feature located at the image origin. Each of the lines described in Fig. 3 can also be identified in Fig. 4 as a boundary to a distinctive pressure region. For clarity, these pressure regions have been labeled to correspond to the labels of the separation lines in Fig. 3. Starting upstream of the jet exit, the lambda shock and bow shock are represented as two curved bands of high pressure that wrap around the injector port. The high-pressure region 1 is caused by the lambda shock and is (spatially) the larger of the two. The foot of the curved bow shock is located between the high-pressure regions 1 and 2. The bow shock causes a significant increase in pressure in region 2 and extends to the front lip of the jet exit [25]. Behind the jet exit, a low-pressure region 4 exists that extends approximately 3.5 jet diameters downstream (along the tunnel centerline). However, low-pressure region 4 extends slightly further downstream for offcenterline axis locations, giving the region a winglike shape. This characteristic has also been reported on by other investigators [25].

C. Planar Imaging

Another flowfield characteristic of interest was the boundary of the jet penetration into the crossflow. Early studies conducted for the transverse injection of a gas into a supersonic freestream have used the height of the Mach disk as a measure of penetration depth [26,27]. In the present work, the penetration boundary was obtained by manually tracking the outer edge of 50 averaged images generated by Mie scattering of condensed ethanol particles that were seeded into the jet. The outer edge was defined as the boundary in which recorded intensity dropped to less than 10% of the maximum seen in the freestream flow. A similar technique has been used by past investigators in visualizing the penetration profile [7]. The results are shown in Fig. 5a as a scatter plot of points collected on the boundary. Ben-Yakar and Hanson [14] discuss a similar method and plot in their work. However, their penetration profile was obtained by tracking the outer edge from schlieren images. In Fig. 5a, the penetration reaches a maximum height of approximately 19.5 mm at a location of six jet diameters downstream of the injector port. At this location, the thickness of the penetration band (i.e., the degree of point scatter in the instantaneous images) is approximately two jet diameters. Ben-Yakar and Hanson [14] report an estimated penetration band thickness of three jet diameters for $J = 1.4$ and a hydrogen jet injected into a supersonic crossflow. For comparison with previous studies, past work has shown a high degree of collapse in the jet

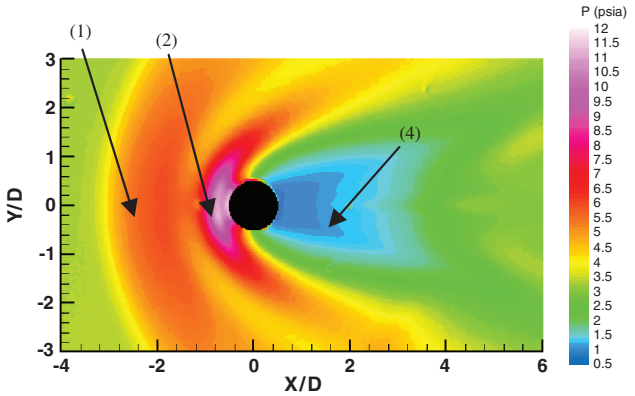

Fig. 4 Surface pressure distribution in the near-jet region, where labels 1, 2, and 4 mark pressures that correspond to the separation lines in Fig. 3.

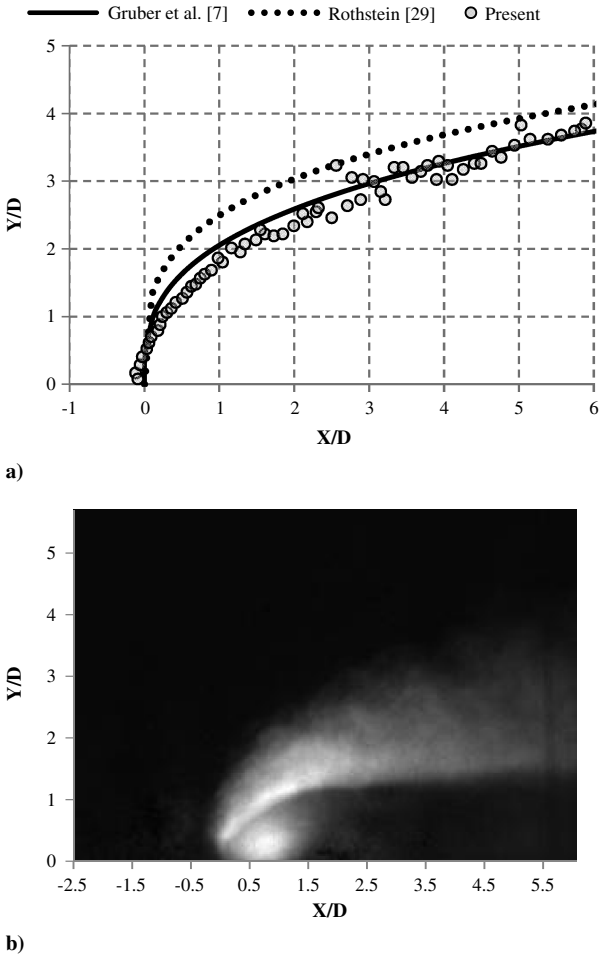

Fig. 5 Mie scattering images from an ethanol seeded jet showing the a) penetration profile boundary plotted against the previous empirical relation by Gruber et al. [7] and Rothstein [29] and b) averaged intensity images from 50 run images.

penetration profile when coordinate axes are scaled by J^{-1} [7,28]. To this end, empirical correlations given by Gruber et al. [7] and Rothstein [29] have also been plotted and are shown in Fig. 5a. The results in Fig. 5a show good agreement with other investigations and suggest validity in the current method for determining the jet penetration profile at this value of J. An averaged intensity image of the jet being seeded with ethanol is also shown Fig. 5b. In Fig. 5b, 50 run images and 50 background images were collected and averaged.

D. Schlieren Imaging

Instantaneous schlieren images were obtained to investigate the distribution of density gradients within the flowfield of a transverse jet. For this study, 200 instantaneous images were collected and phase-averaged. Although the flowfield was investigated with the knife edge in the horizontal and vertical arrangements, only images in the vertical orientation are presented. The images in the vertical arrangement were selected because of the suppression of the vertical density gradients due to the boundary layer, allowing key features of the flowfield to be more easily visualized [30]. The resulting images (instantaneous and phase-averaged) for the unperturbed flow are shown in Fig. 6. The flow is from left to right, and the incoming boundary layer is identified in Fig. 6a. Several weak waves can also be identified in Fig. 6. These weak waves were formed from minor surface discontinuities in the test section walls and are common in most supersonic wind-tunnel facilities. Their presence did not appear to influence the results presented in any significant manner. In Fig. 6b, distinct flowfield features in the near-jet region have also been labeled; specifically, the lambda shock, the barrel shock, the bow shock, and the Mach disk.

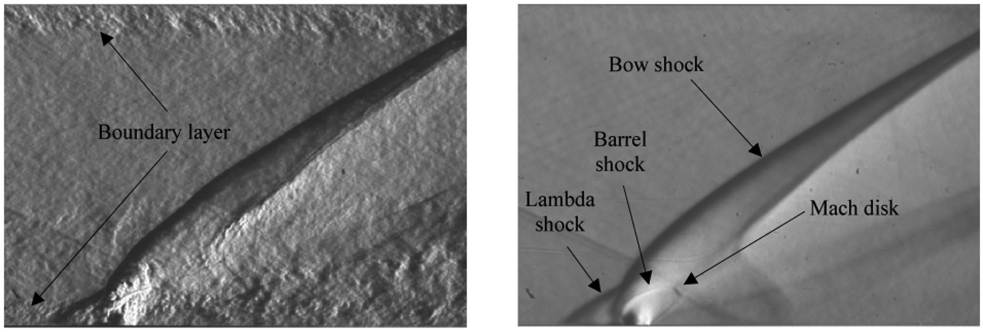

a) b)

Fig. 6 Schlieren images of a sonic transverse jet in a supersonic crossflow: a) instantaneous and b) time-averaged.

The experimental study for the flowfield following the excitation pulse was conducted for incremental delay times ranging from 5–120 μs from the laser energy input at the jet exit. Phase-averaged schlieren images are illustrated in Fig. 7 for selected delay times from the excitation pulse. Also, for the images in Fig. 7, the excitation pulse was located at a transverse position of 0D from the jet exit (i.e., directly at the jet exit). Although schlieren imaging was conducted for the remaining two vertical positions of the excitation pulse (1.5D and 3D), similar results were observed for each of the three cases. Moreover, the 0D case most clearly illustrated the interaction between the excitation pulse and relevant flowfield features. All three cases will be considered and compared in the velocity data section to

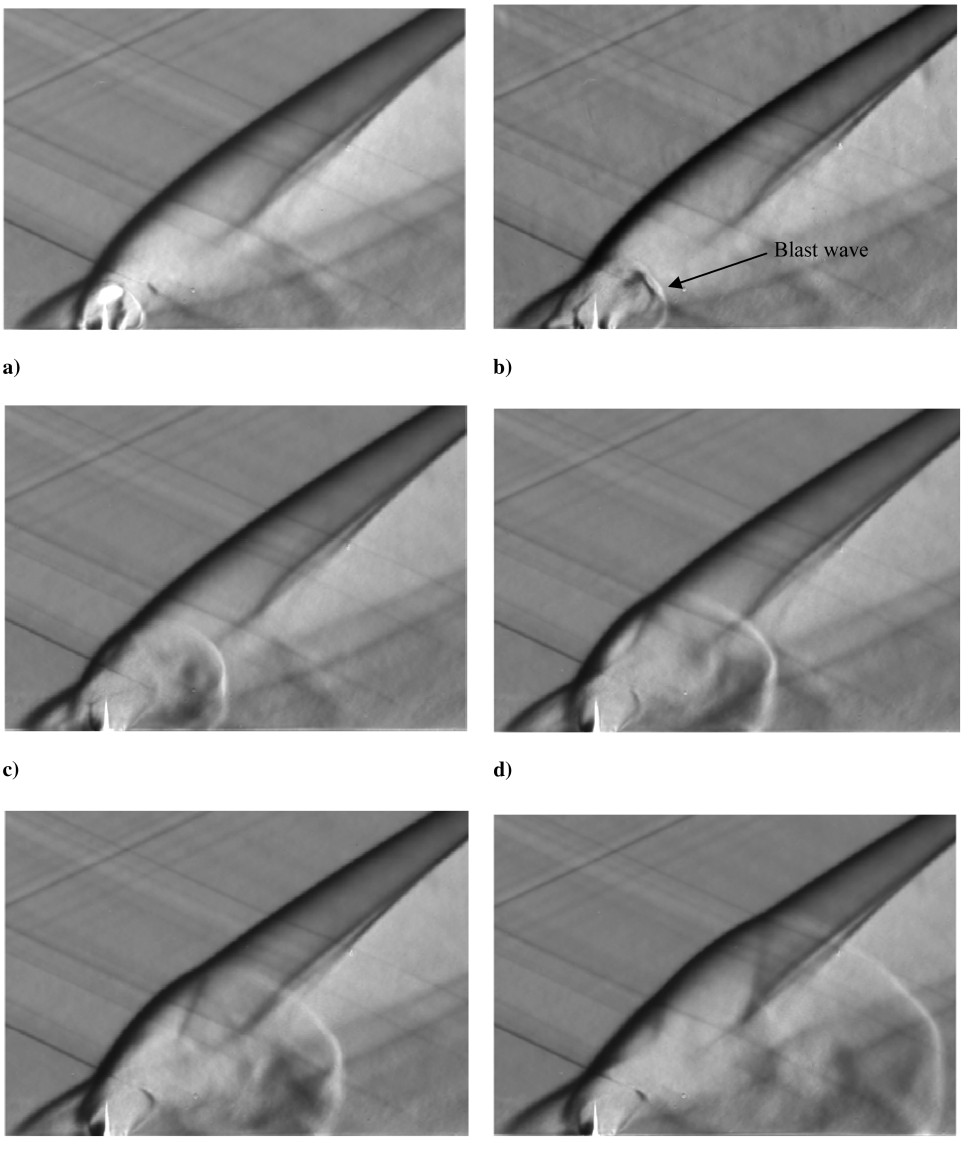

a) b)

c) d)

e) f)

Fig. 7 Phase-averaged schlieren images at selected delay times from a 200 mJ energy input at a 0D vertical location: a) 5, b) 10, c) 20, d) 30, e) 40, and f) 60 μs.

follow. Apparent in all the images, the flowfield features as described for Fig. 6b can be identified. Figure 7a corresponds to a 5 μs delay from the excitation pulse. In this image, the blast wave from the laser pulse originates at the jet exit and is distorted by the relative velocity internal and external to the jet. At this point, the disturbance has not significantly propagated through the flow. In Figs. 7b and 7c, the delay time between excitation and imaging was increased to 10 and 20 μs, respectively. At these increased times, the disturbance from the laser pulse, which first appeared as a single thermal spot, has traversed through the flowfield, altering some of the characteristics seen in the unperturbed flow. The propagation of the blast wave through the flowfield has disrupted the structure of the barrel shock and the Mach disk and can be seen reforming in Figs. 7d–7f.

E. Particle Image Velocimetry

In addition to the schlieren imaging, PIV was conducted to determine the two-component velocity field for the jet in crossflow (with and without excitation) and to determine the incoming boundary-layer thickness δ without the jet operating. For all PIV images presented, the streamwise and transverse axes have been similarly nondimensionalized by the jet exit diameter, as in Figs. 3 and 4. The jet exit is also, again, located at the origin of the image, or the coordinates $(x/D, y/D) = (0, 0)$.

For measurement of the incoming boundary-layer thickness, the test section model was replaced with a smooth top-wall assembly not containing the transverse jet orifice. Also, in constructing the boundary-layer thickness, ensemble averages of 1344 image pairs were used. The results are presented as color contours for the average streamwise velocity component, as shown in Fig. 8a. In Fig. 8a, although velocities only as low as 70% of the freestream velocity were measured, the transition from slower velocities near the wall to freestream conditions can still be observed. From these velocity data, a boundary-layer profile was constructed and is illustrated in Fig. 8b. A boundary-layer thickness δ_{99} was also calculated, based on the position of 99% of the freestream velocity. Under this approach, the boundary-layer thickness upstream of the jet was determined to be approximately $\delta_{99} = 3.05$ mm (± 0.13 mm, based on measurement resolution), where the current experimental arrangement was capable of resolving velocity vectors within 200 μm of the surface. It should also be noted that the boundary-layer thickness is close to the jet exit diameter, which, while common for similar studies, will affect flowfield characteristics, such as the bow shock and upstream recirculation zone.

In the analysis of the unperturbed flow, ensemble averages of 640 image pairs were used. The results are presented in Fig. 9 as color contours for the average streamwise and transverse velocity, along with their rms components. Corresponding streamlines have also been superimposed on the image of the average streamwise velocity (Fig. 9a) and vectors for the image of the average transverse velocity (Fig. 9b). As can be seen in the images in Fig. 9, the PIV system was capable of resolving several of the features seen in the schlieren images, which are typical of a transverse jet flowfield. Among these are the lambda shock, the bow shock, the barrel shock, and the Mach disk. Each of these has been labeled in Fig. 9. However, for the last two features, because of the scarcity of flow-tracking particles in the near-jet region (due to the flowfield dynamics) and the resolution of the subregions used to calculate the PIV vectors, the barrel shock and Mach disk were imaged with limited detail. Also, it is important to note that the particles used for PIV, although small, still have a slight lag time in tracking the fluid. This is particularly evident across the sharp velocity gradients found through shock waves. To this end, only the relative position and size of these features can be inferred from the velocity images, with little information on their internal structures.

For the jet flowfield following the disturbance from the excitation pulse, two-component contour plots were generated for the vorticity field. However, in contrast to the images in Fig. 9, the view was shifted almost three jet diameters downstream of the spot where the forcing was introduced to protect the CCD camera from the intense laser light in that area. As a means of comparison, vorticity field images of the unperturbed flow, for both the full and shifted fields of view, are shown in Fig. 10. As in Fig. 9, for both images shown in Fig. 10, the vorticity values have again been nondimensionalized by the freestream velocity and the jet exit diameter. In Fig. 10a, the full view of the transverse jet flowfield is shown, in which it can be seen that the highest values of vorticity are within a region of 1–2 jet diameters of the jet exit. A layer of increased vorticity, however, does persist further downstream of the jet exit but with decreasing intensity. In Fig. 10b, a shifted (and slightly zoomed in) view of the vorticity field is shown. The streamlines for several coherent structures detected in the unperturbed flowfield have also superimposed onto Fig. 10b to serve as a baseline for the flowfield with forcing applied.

In identifying large-scale structures, taking after Adrian et al. [31], the definition of a vortex offered by Kline and Robinson [32] was used: "A vortex exists when instantaneous streamlines mapped onto a plane normal to the core exhibit a roughly circular or spiral pattern, when viewed in a reference frame moving with the center of the vortex core." Accordingly, two necessary conditions are that the velocity field must be viewed in a convective reference frame and that the vorticity must be concentrated in the core of the structure. However, vorticity not only identifies vortex cores but also shearing motions that may be also present in a flow [31]. Again, taking after Adrian et al. [31], a number of methods have been developed for identifying locations of vortices and calculating vortex statistics from the critical-point analysis of the local velocity gradient and its corresponding eigenvalues. In view of a three-dimensional field, the local velocity gradient tensor will have one real eigenvalue λ_r and a pair of complex conjugate eigenvalues $(\lambda_{cr} \pm i\lambda_{ci})$ when the discriminant of its characteristic equation is positive. As discussed by Chong et al. [33], when this condition holds valid, the particle trajectories about the eigenvector corresponding to the eigenvalue λ_r exhibit a swirling, spiral motion, where the quantity $(\lambda_{ci})^{-1}$ represents the period for a particle to swirl once about the λ_r axis. Zhou et al. [34,35] have further shown that λ_{ci} quantifies the strength

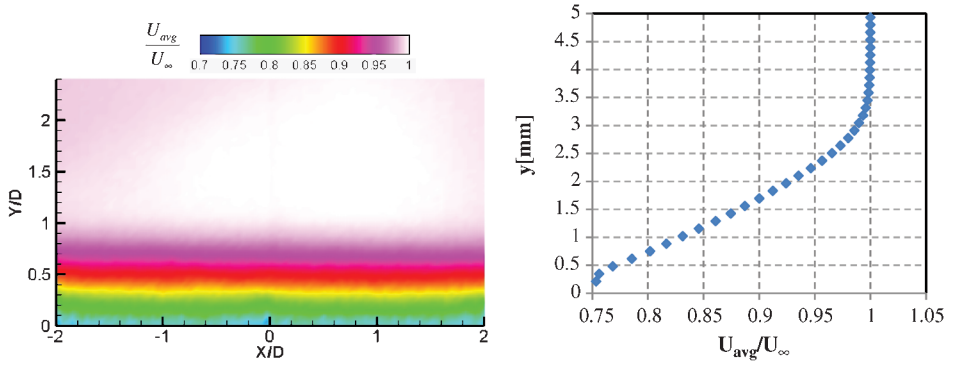

a) b)

Fig. 8 Boundary-layer illustrations using a) color contours of the average streamwise velocity and b) a spatially averaged profile.

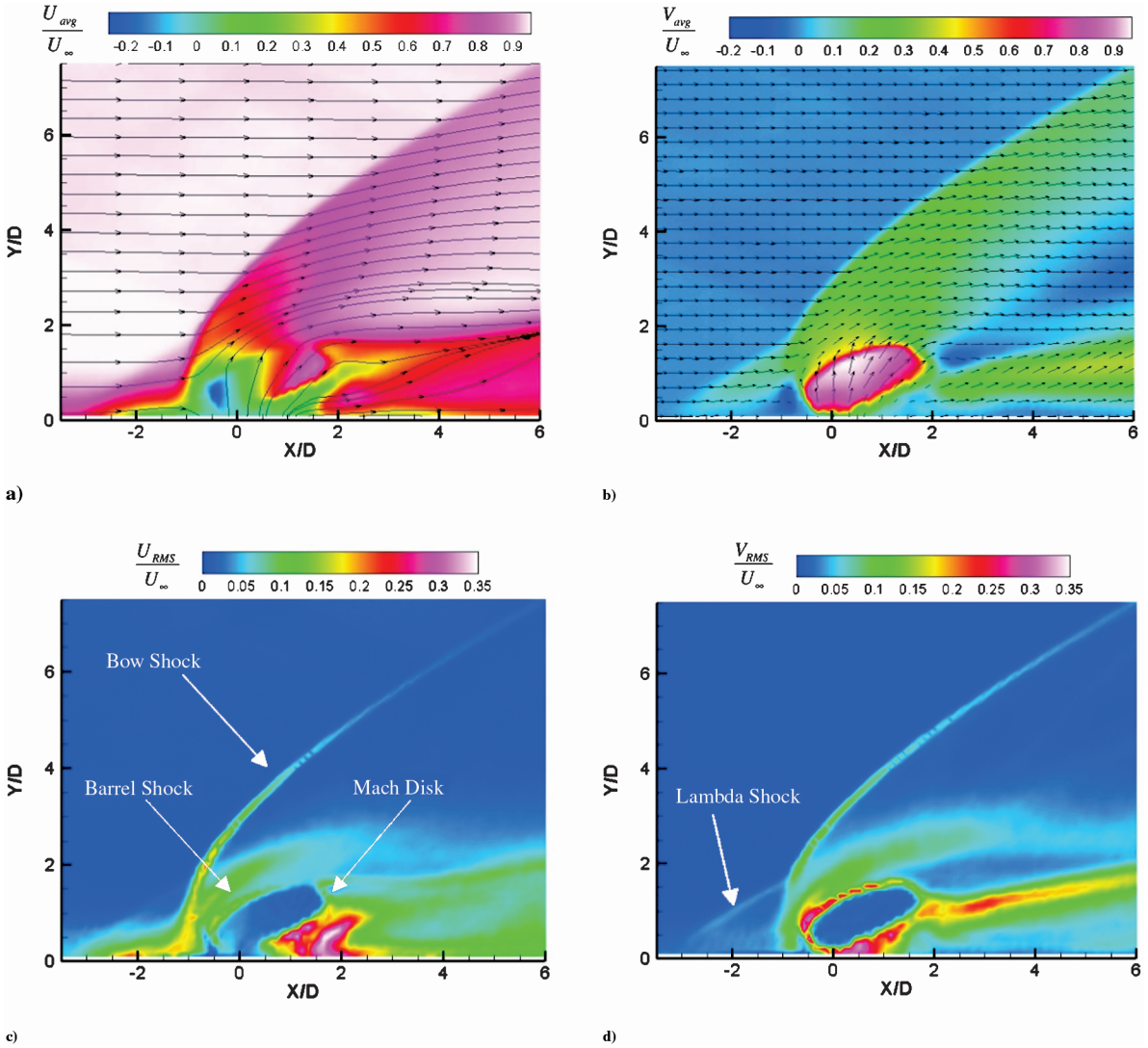

Fig. 9 Sonic transverse jet in a supersonic crossflow: a) average streamwise velocity, b) average transverse velocity, c) streamwise rms velocity, and d) transverse rms velocity.

of any swirling motion and, hence, defined λ_{ci} as the swirling strength of a vortex. For a two-dimensional PIV field, an equivalent form of the three-dimensional local velocity gradient tensor can be computed in the plane, in which the PIV data lie from the following equation:

$$\underline{D}^{2-D} = \begin{bmatrix} \frac{\partial u_1}{\partial x_1} & \frac{\partial u_1}{\partial x_2} \\ \frac{\partial u_2}{\partial x_1} & \frac{\partial u_2}{\partial x_2} \end{bmatrix} \tag{2}$$

where (x_1 and x_2) are the streamwise and transverse directions and (u_1 and u_2) are the corresponding velocities. Equation (2) will have either two real eigenvalues or a pair of complex conjugate eigenvalues. Regions in which vortices exist can then be identified by plotting isoregions of $\lambda_{ci} > 0$. Moreover, the swirling motion in these regions can be observed by performing a local Galilean decomposition in the immediate vicinity of peaks in swirling strength [31]. For the present work, Eq. (2) was computed using a second-order central-difference scheme for interior points and second-order forward-differencing and backward-differencing schemes for the boundary points. Isoregions for which $\lambda_{ci} > 0$ were then identified and plotted in a convective reference frame. The convective velocity was determined by the corresponding velocity at the location of peak swirling strength for a given isoregion. Additional details in vortex detection and visualization can be found in [31].

For the flowfield including the excitation pulse, based on the results shown by the schlieren images, four delay times from the laser energy input at the jet exit were selected for investigation with PIV. This included delay times of: 20, 40, 60, and 80 μs, respectively. Velocity field data from PIV were also obtained at these delay times for each of the three excitation positions relative to the jet exit. Again, this was at vertical distances of the excitation pulse from the jet exit of 0, 1.5, and 3 jet diameters and, in each case, centered along the exit centerline. Vorticity plots for the three cases are shown in Fig. 11. As for the unperturbed case in Fig. 10, streamlines for coherent structures within the flowfield were calculated and superimposed onto the images. The method described previously for visualizing vortices was again used; however, only vortices that were not observed in the base flow were considered. Furthermore, vortices with a peak swirling strength of less than 25% of the maximum swirling strength seen in the unperturbed flowfield were ignored. The threshold value was selected a priori to capture only the dominant structures induced into the flow through the excitation pulse. This approach also helped to eliminate any remnants of instantaneous features of the flowfield that were not completed removed by averaging image pairs.

Beginning with the 0D case, in Fig. 11a, a single vortex was visualized in the flowfield at 20 μs; this vortex has been labeled as I_{0D}. A circular region of increased positive vorticity can also be observed entering the field of view at the approximate coordinates of $(x/D, y/D) = (2, 2)$. Both of these features occurred in the wake of the blast wave from the excitation pulse, for which the location is depicted as a curved black line in Fig. 11a. By 40 μs, Fig. 11b, five additional vortices developed in the flowfield; however, only one of these vortices (labeled II_{OD}) remained coherent and persisted in the

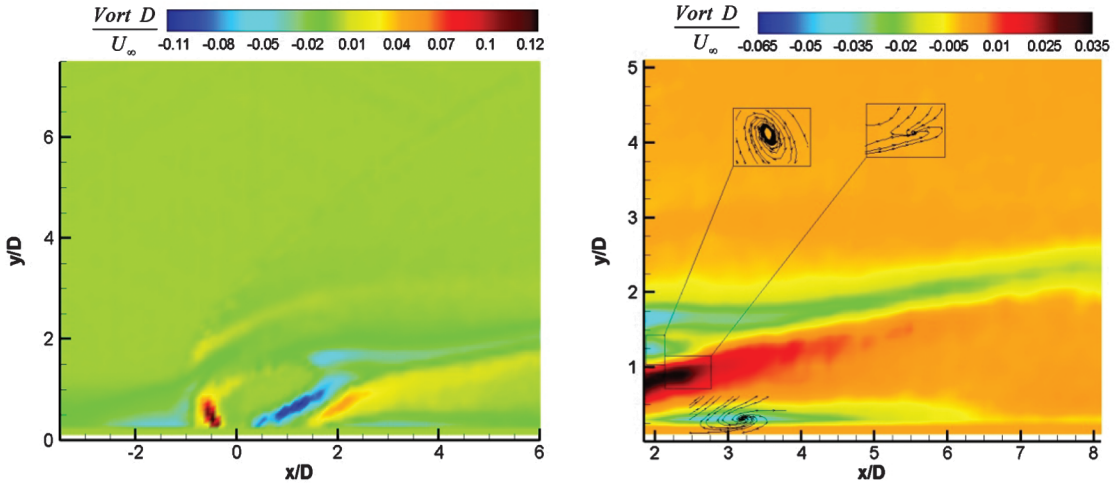

Fig. 10 Vorticity contour plots for a) full and b) shifted fields of view for the unperturbed flowfield.

flow for increased delay times. This can be seen in Figs. 11c and 11d for the increased delay times of 60 and 80 μs. The dark circular region of increased positive vorticity in Fig. 11a, can also be identified in Fig. 11b, separating vortices I_{OD} and II_{OD}.

Vorticity contour plots for the excitation location of 1.5D are shown in Figs. 11e–11h. The four selected delay times (20, 40, 60, and 80 μs) are again considered, where Fig. 11e corresponds to the flowfield at 20 μs after the excitation pulse. In contrast to the 0D case,

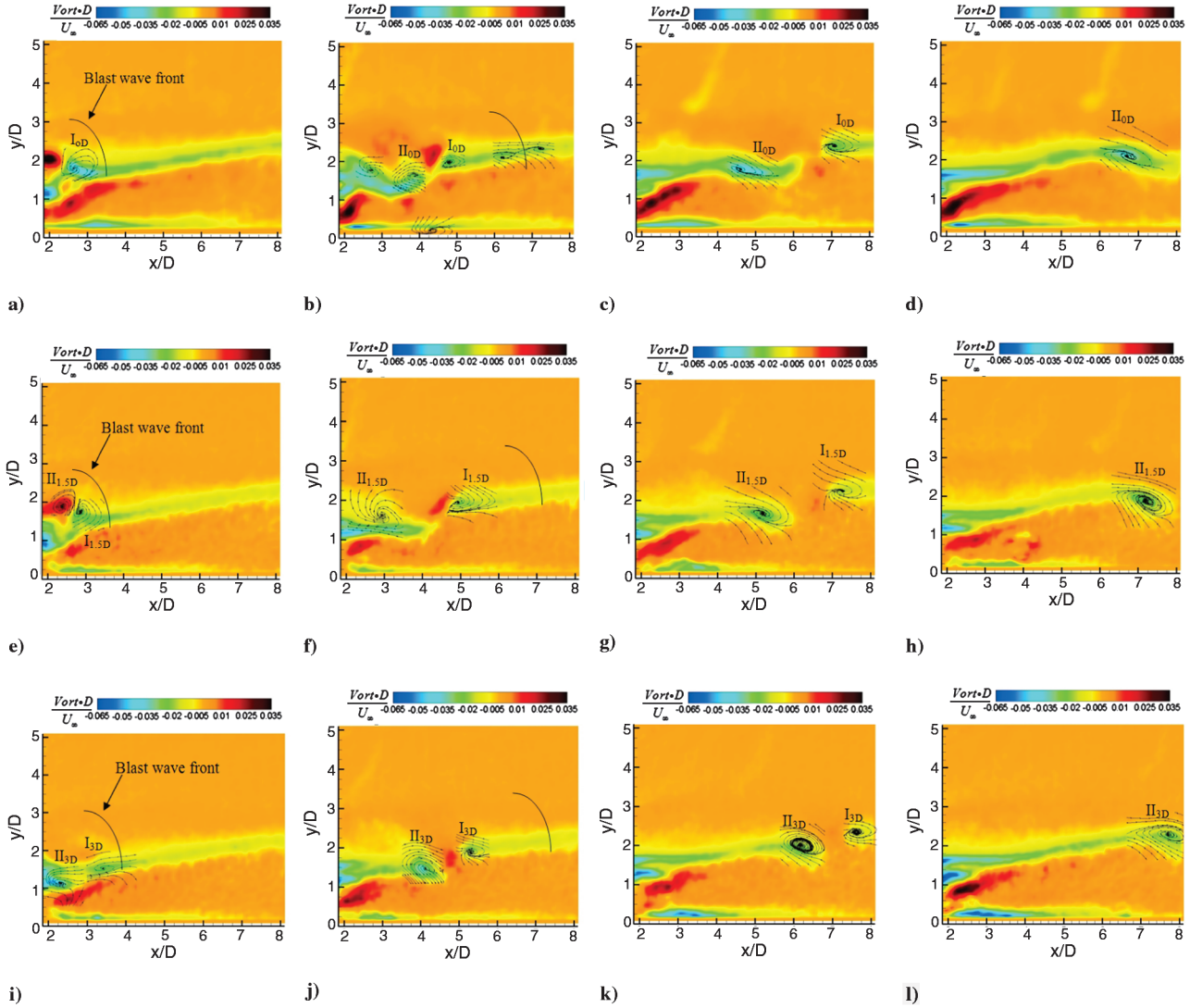

Fig. 11 Vorticity contour plots for a 200 mJ laser excitation pulse at locations of 0D (top row), 1.5D (middle row), and 3D (bottom row) and at delay times of 20 (1st column), 40 (2nd column), 60 (3rd column), and 80 μs (4th column).

two vortices (labeled $I_{1.5D}$ and $II_{1.5D}$) were identified at this delay time, and the front edge of the blast wave was positioned at a slightly further downstream location. The dark circular region of increased positive vorticity, seen in Fig. 11a, is also apparent in Fig. 11e but with less intensity. It was not clear if this was due to its slightly further downstream position in the flowfield or through a different mechanism. At 40 μs, a relatively large gap (in comparison to the 0D case) develops between vortices $I_{1.5D}$ and $II_{1.5D}$. While, at this delay time, the position of $II_{1.5D}$ correlates well with II_{0D}, the center of vortex $I_{1.5D}$ is located almost one jet diameter upstream of I_{0D}. Vortices $I_{1.5D}$ and $II_{1.5D}$ both persist in the flow for increased delay time (Figs. 11g and 11h), and their locations continue to be slightly downstream of those observed for the 0D case.

Last, vorticity contour plots for the vertical location of 3D are shown in Fig. 11i–11l. From Fig. 11i, two vortices (labeled I_{3D} and II_{3D}) formed in the flowfield at a 20 μs delay time. Consistent with the trends from the 1.5D case, lowering the position of the excitation pulse into the flowfield resulted in the center of both the vortices and the location of the blast wave having a slightly more downstream position. The circular region of increased positive vorticity seen in the 0D and 1.5D case, however, was not observed for the 3D case. This region first appeared in Fig. 11j, separating the two vortices. In Fig. 11j, both vortices appear with a further downstream position (in comparison with the previous two cases) but with less of a separation gap than in the 1.5D case. Vortices I_{3D} and II_{3D} continue to convect downstream in Figs. 11k and 11l, with increasing delay time.

As a means of further quantifying the behavior of the vortices seen in Fig. 11, as well as their relative strength, plots of the streamwise position and period required for a particle to swirl once about the λ_r axis are given in Fig. 12. In Fig. 12, only vortices $I_{0D,1.5D,3D}$ (vortex I) and $II_{0D,1.5D,3D}$ (vortex II) are considered and at delay times for which they can be compared for the three vertical excitation positions. The streamwise positions (nondimensionalized by the jet exit diameter) of the vortices are shown as a function of the delay time in Fig. 12a. This plot confirms the observations made from vorticity contour plots in Fig. 11; specifically, as the excitation pulse is introduced at lower positions below the jet exit, the vortices are either forming earlier or convecting through the flowfield at an increased rate. While the data suggest the former for vortex I and the latter for vortex II, it is difficult to infer any trends, since only three points are being compared. However, while the mechanism is not completely clear, the results in Fig. 12a illustrate that the induced structures are being shifted downstream as the plasma pulse is introduced at positions further below the jet exit.

The periods required for a particle to swirl once about the λ_r axis for both vortices are similarly shown as a function of delay time in Fig. 12b. The values in Fig. 12b have been nondimensionalized by the vortex with the shortest period (or highest swirling strength) seen in the unperturbed flowfield, shown in Fig. 10b. The shortest period calculated from the unperturbed flowfield in Fig. 10b was approximately $(\lambda_{ci,\text{unperturbed}})^{-1} = 12.47\ \text{ms}^{-1}$. In Fig. 12b, similar trends can be observed for the vortices induced with the excitation pulse located at vertical positions of 0D and 1.5D. For these two cases, while, for vortex II, the period is decreasing in time, the opposite behavior is seen for vortex I. Then, for the case of the excitation pulse located at the vertical positions of 3D, the period increases in time for both vortices I and II. This suggests that the swirling strength of the induced vortices are dependent upon its relative position of the excitation pulse to the jet exit.

IV. Conclusions

In the present work, a detailed analysis of a sonic transverse jet in a supersonic Mach 2.25 crossflow was conducted with flow oil visualizations, PSP measurements, schlieren photography, and two-component velocity field data. The broad array of measurement techniques used is not only valuable to further quantify characteristics of the flowfield but will also provide valuable quantitative information for comparison with future computational modeling efforts. In addition to defining the unperturbed flow, the influence of laser excitation to the flowfield was also examined. The different diagnostics used revealed that the energy pulse disrupted the barrel shock and Mach disk of the flowfield and caused a perturbation to the jet-shear layer. This perturbation resulted in the formation of several vortices, two of which remained coherent for the flow times considered. Significant differences were also observed for introducing the excitation and different positions in the flow, relative to the jet exit. These results suggest the possibility of using laser excitation as a control technique for mixing applications that involve a transverse jet flowfield. However, further studies are needed to define the parameters of the forcing that result in the most optimized flowfield, as well as further quantify the influence on mixing. Among many others, these include the power of the laser pulse and the repetition rate. Additional studies are also needed to further investigate the interaction between the jet and the plasma pulse. In particular, the energy pulse affects the local jet density and causes the jet spread to be different from that of a continuously injected low jet. However, the effect needs to be further quantified and the underlying physics better understood.

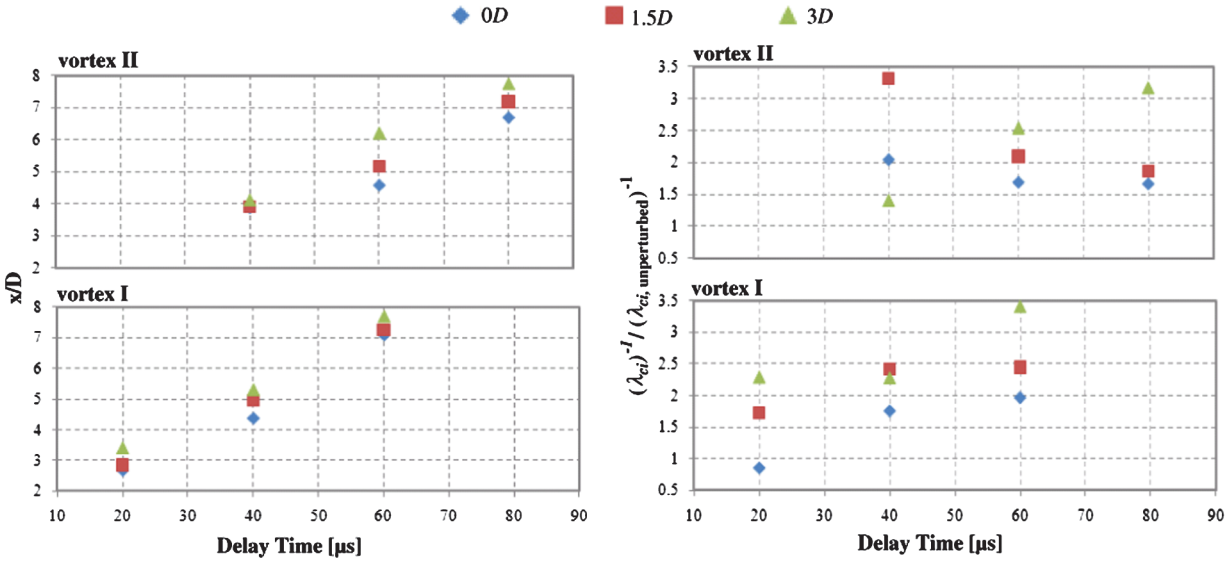

a) b)

Fig. 12 Vortices $I_{0D,5D,3D}$ (vortex I) and $II_{0D,5D,3D}$ (vortex II): a) streamwise position and b) period required for a particle to swirl once about the λ_r axis.

Acknowledgments

The authors would like to thank the U.S. Air Force Office of Scientific Research (AFOSR), with John Schmisseur, for funding this work on energy deposition for local flow control (FA9550-07-1-0215). Any opinions, findings, and conclusions or recommendations expressed in the material are those of the authors and do not necessarily reflect the views of AFOSR.

References

[1] Shapiro, S. R., King, J. M., M'Closkey, R. T., and Karagozian, A. R., "Optimization of Controlled Jets in Crossflow," *AIAA Journal*, Vol. 44, No. 6, 2006, pp. 1292–1298. doi:10.2514/1.19457

[2] Cubbison, R. W., Anderson, B. H., and Ward, J. J., "Surface Pressure Distributions with a Sonic Jet Normal to Adjacent Flat Surfaces at Mach 2.92 to 6.4," NASA TN D-580, 1961.

[3] Janos, J. J., "Loads Induced on a Flat-Plate Wing by an Air Jet Exhausting Perpendicularly Through the Wing and Normal to a Free-Stream Flow of Mach Number 2.0," NASA TN D-649, 1961.

[4] Kim, C.-K., Yu, S.-T. J., and Zhang, Z.-C., "Cavity Flow in Scramjet Engine by Space-Time Conservation and Solution Element Method," *AIAA Journal*, Vol. 42, No. 5, 2004, pp. 912–919. doi:10.2514/1.9017

[5] Ben-Yakar, A., Mungal, M. G., and Hanson, R. K., "Time Evolution and Mixing Characteristics of Hydrogen and Ethylene Transverse Jets in Supersonic Crossflows," *Physics of Fluids*, Vol. 18, No. 2, 2006, p. 026101. doi:10.1063/1.2139684

[6] Alves, L. S., Kelly, R. E., and Karagozian, A. M., "Local Stability Analysis of an Inviscid Transverse Jet," *Journal of Fluid Mechanics*, Vol. 581, 2007, pp. 401–418. doi:10.1017/S0022112007005873

[7] Gruber, M. R., Nejad, A. S., Chen, T. H., and Dutton, J. C., "Mixing and Penetration Studies of Sonic Jets in a Mach 2 Freestream," *Journal of Propulsion and Power*, Vol. 11, No. 2, 1995, pp. 315–323. doi:10.2514/3.51427

[8] VanLerberghe, W. M., Santiago, J. G., Dutton, J. C., and Lucht, R. P., "Mixing of a Sonic Transverse Jet Injected into a Supersonic Flow," *AIAA Journal*, Vol. 38, No. 3, 2000, pp. 470–479. doi:10.2514/2.984

[9] Srinivasan, R., and Bowersox, R., "Simulation of Transverse Gaseous Injection Through Diamond Ports into a Supersonic Freestream," *Journal of Propulsion and Power*, Vol. 23, No. 4, 2007, pp. 772–782. doi:10.2514/1.18405

[10] Fric, T. F., and Roshko, A., "Vortical Structure in the Wake of a Transverse Jet," *Journal of Fluid Mechanics*, Vol. 279, No. 25, 1994, pp. 1–47. doi:10.1017/S0022112094003800

[11] Ben-Yakar, A., and Hanson, R. K., "Experimental Investigation of Flame-Holding Capability of a Transverse Hydrogen Jet in Supersonic Cross-Flow," *Proceedings of the 27th International Symposium on Combustion*, Combustion Inst., Pittsburgh, PA, 1998, pp. 2173–2180.

[12] Gruber, M. R., Nejad, A. S., Chen, T. H., and Dutton, J. C., "Bow Shock/Jet Interaction in Compressible Transverse Injection Flowfields," *AIAA Journal*, Vol. 34, No. 10, 1996, pp. 2191–2193. doi:10.2514/3.13372

[13] Gruber, M. R., Nejad, A. S., Chen, T. H., and Dutton, J. C., "Large Structure Convection Velocity Measurements in Compressible Transverse Injection Flowfields," *Experiments in Fluids*, Vol. 22, No. 5, 1997, pp. 397–407. doi:10.1007/s003480050066

[14] Ben-Yakar, A., and Hanson, R. K., "Ultra-Fast-Framing Schlieren System for Studies of the Time Evolution of Jets in Supersonic Crossflows," *Experiments in Fluids*, Vol. 32, No. 6, 2002, pp. 652–666. doi:10.1007/s00348-002-0405-z

[15] Murugappan, S., Gutmark, E., Carter, C., Dunbar, J., Gruber, M., and Hsu, K.-Y., "Transverse Supersonic Controlled Swirling Jet in a Supersonic Cross Stream," *AIAA Journal*, Vol. 44, No. 2, 2006, pp. 290–300. doi:10.2514/1.13312

[16] Billig, F. S., Orth, R. C., and Lasky, M., "A Unified Analysis of Gaseous Jet Penetration," *AIAA Journal*, Vol. 9, No. 6, 1971, pp. 1048–1058. doi:10.2514/3.49916

[17] Kawai, S., and Lele, S., "Mechanisms of Jet Mixing in a Supersonic Crossflow: A Study Using Large-Eddy Simulation," AIAA Paper 2008-4575, 2008.

[18] Santiago, J. G., and Dutton, J. C., "Velocity Measurements of a Jet Injected into a Supersonic Crossflow," *Journal of Propulsion and Power*, Vol. 13, No. 2, 1997, pp. 264–273. doi:10.2514/2.5158

[19] Swanson, Taylor, "Interaction of Laser Energy Deposition with a Normal Shock," M.S. Thesis, Univ. of Illinois, Urbana-Champaign, IL, 2006.

[20] Zhuang, N., Alvi, F. S., Alkislar, M. B., and Shih, C., "Supersonic Cavity Flows and their Control," *AIAA Journal*, Vol. 44, No. 9, 2006, pp. 2118–2128. doi:10.2514/1.14879

[21] Humphreys, W. M., and Bartram, S. M., "Measurement of Separating Flow Structures Using a Multiple-Camera DPIV System," *19th International Congress on Instrumentation in Aerospace Simulation Facilities*, NASA, 2001.

[22] Urban, W. D., and Mungal, M. G., "Planar Velocity Measurements in Compressible Mixing Layers," *Journal of Fluid Mechanics*, Vol. 431, 2001, pp. 189–222. doi:10.1017/S0022112000003177

[23] Huffman, R., "An Experimental Investigation into the Effect of Plasma on the Flow Features of an Axisymmetric Jet," Ph.D. Dissertation, Univ. of Illinois, Urbana-Champaign, IL, 2006.

[24] Grant, I., and Owens, E., "Confidence Interval Estimates in PIV Measurements of Turbulence Flows," *Applied Optics*, Vol. 29, No. 10, 1990, pp. 1400–1402. doi:10.1364/AO.29.001400

[25] Everett, D. E., Woodmansee, M. A., Dutton, J. C., and Morris, M. J., "Wall Pressure Measurements for a Sonic Jet Injected Transversely into a Supersonic Crossflow," *Journal of Propulsion and Power*, Vol. 14, No. 6, 1998, pp. 861–868. doi:10.2514/2.5357

[26] Schetz, J. A., Weinraub, R. A., and Mahaffey, R. E., "Supersonic Transverse Injection into a Supersonic Stream," *AIAA Journal*, Vol. 6, No. 5, 1968, pp. 933–934. doi:10.2514/3.4631

[27] Schetz, J. A., Hawkins, P. F., and Lehman, H., "Structure of Highly Underexpanded Transverse Jets in a Supersonic Stream," *AIAA Journal*, Vol. 5, No. 5, 1967, pp. 882–884. doi:10.2514/3.4095

[28] Keffer, J. F., and Baines, W. D., "The Round Turbulent Jet in a Cross-Wind," *Journal of Fluid Mechanics*, Vol. 15, No. 4, 1963, pp. 481–496. doi:10.1017/S0022112063000409

[29] Rothstein, A. D., "A Study of the Normal Injection of Hydrogen into a Heated Supersonic Flow Using Planar Laser-Induced Fluorescence," M.S. Thesis, Massachusetts Inst. of Technology, Cambridge, MA, 1991.

[30] Murray, R. C., and Elliott, G. S., "Characteristics of the Compressible Shear Layer over a Cavity," *AIAA Journal*, Vol. 39, No. 5, 2001, pp. 846–856. doi:10.2514/2.1388

[31] Adrian, R. J., Christensen, K. T., and Liu, Z.-C., "Analysis and Interpretation of Instantaneous Turbulent Velocity Field," *Experiments in Fluids*, Vol. 29, No. 3, 2000, pp. 275–290. doi:10.1007/s003489900087

[32] Kline, S. J., and Robinson, S. K., "Quasi-Coherent Structures in the Turbulent Boundary Layer. Part I: Status Report on a Community-Wide Summary of the Data," *Proceedings of Zaric Memorial Conference in Near-Wall Turbulence*, Hemisphere, New York, 1989, pp. 200–217.

[33] Chong, M. S., Perry, A. E., and Cantwell, B. J., "A General Classification of Three-Dimensional Flow Fields," *Physics of Fluids A*, Vol. 2, No. 5, 1990, pp. 408–420. doi:10.1063/1.857730

[34] Zhou, J., Adrian, R. J., and Balachandar, S., "Autogeneration of Near-Wall Vortical Structures in Channel Flow," *Physics of Fluids*, Vol. 8, No. 1, 1996, pp. 288–290. doi:10.1063/1.868838

[35] Zhou, J., Adrian, R. J., Balachandar, S., Kendall, T. M., "Mechanisms for Generating Coherent Packets of Hairpin Vortices in Channel Flow," *Journal of Fluid Mechanics*, Vol. 387, 1999, pp. 353–359. doi:10.1017/S002211209900467X

N. Chokani
Associate Editor